Customized CMOS wavefront sensor

Davies W. de Lima Monteiro[*a], Gleb Vdovin[a], J. Gerardo Rocha[b], Ventzeslav Iordanov[a], Mikhail Loktev[a] and Pasqualina Sarro[a]
[a]EI Lab. ITS / DIMES - Delft University of Technology, The Netherlands;
[b]Industrial Electronics Dept. - University of Minho, Portugal

ABSTRACT

We report on an integrated Hartmann wavefront sensor (WFS) using passive-pixel architecture and pixels clustered as position-sensitive detectors for dynamic wavefront analysis. This approach substitutes a conventional imager, such as a CCD or CMOS imager, by a customized detector, thus improving the overall speed performance. CMOS (complementary-metal-oxide-semiconductor) technology enables on-chip integration of several analog and digital circuitry. The sensor performance depends on the feature size of the technology, noise levels, photosensitive elements employed, architecture chosen and reconstruction algorithm.

Keywords: Wavefront sensor, adaptive optics, position-sensitive detector PSD, passive-pixel, CMOS.

1. INTRODUCTION

As a diagnostic tool a wavefront sensor (WFS) can be used, for instance, in optical shop testing, analysis of fluid dynamics or ophthalmology to detect aberrations on the eye cornea [1, 2, 3]. When part of a close-loop Adaptive Optics system, it is coupled to an adaptive mirror [4, 5] to improve the quality of a light beam or any image propagating through the same path. Dynamic correction at rates higher than 100Hz are demanded for real-time applications.

The Hartmann method (and also the Hartmann-Shack method [6]) allows real-time operation both in open and close loop. It basically samples an incoming wavefront into several spots, by means of a mask with symmetrical holes (Figure 1). If the reference wavefront is flat, the centroid of each spot will be located exactly under the center of each hole. On the other hand, when an aberrated wavefront is sampled, each spot is displaced from the reference position and each spot displacement is proportional to the corresponding local wavefront tilt (Figure 2). Once one knows all displacements, one is either able to smoothly reconstruct the wavefront shape or to appropriately drive the mirror so to correct for the aberrations.

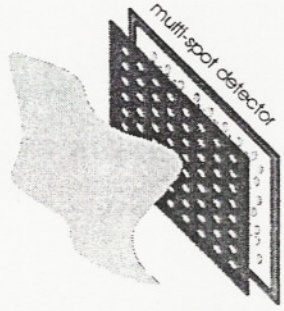

Figure 1: Hartmann method. An aberrated wavefront is sampled into a number of spots by a mask with holes. Spots positions are proportional to local tilts.

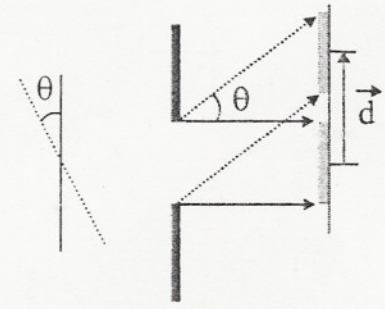

Figure 2: Cross-section of one hole of the Hartmann mask. The effect of local tilt on the spot position is shown.

* contact davies@ei.et.tudelft.nl; Phone/Fax: +31 15 2786285/5755; Electronic Instrumentation Laboratory 13e, Faculty of Information Technology and Systems – TU-Delft, Mekelweg 4, 2628CD Delft, The Netherlands.

High-Resolution Wavefront Control: Methods, Devices, and Applications III, John D. Gonglewski, Mikhail A. Vorontsov, Mark T. Gruneisen, Editors, Proceedings of SPIE Vol. 4493 (2002)
© 2002 SPIE. · 0277-786X/02/$15.00

Operational speed is basically limited to the rate at which one is able to determine all spot displacements. Traditionally CCD's (and more recently CMOS imagers) are used as the multi-spot detector and an image of the spots is first grabbed and then positions are found with a data-reduction algorithm. Nevertheless, off-the-shelf imagers are confined to about 30 fps at their best and position-tracking algorithms usually further limits the overall rate to meager 10 Hz. An alternative method is to use one position-sensitive detector (PSD) [7] per spot (Figure 3). Such a detector usually delivers four signals with which one can easily compute the centroid position (Figure 4). Therefore, time-consuming data-reduction algorithm is replaced by a simple spot centroid calculation.

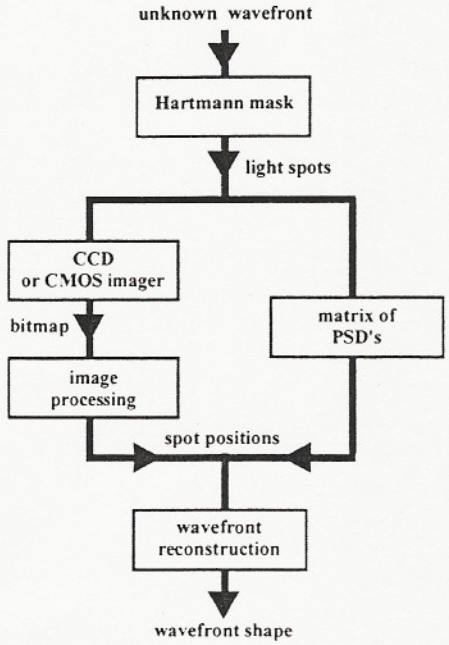

Figure 3: Wavefront sensing and reconstruction. The left branch addresses the conventional flow, whereas the right branch considers a matrix of PSD's as the detector, thus skipping the image processing.

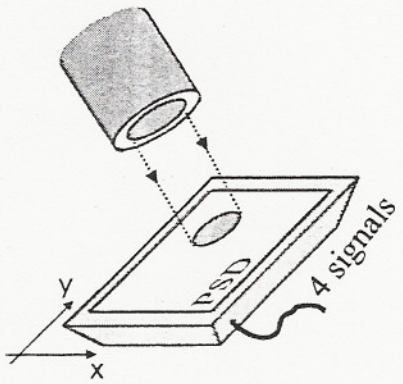

Figure 4: Illustration of a generic optical position-sensitive detector (PSD). X and Y coordinates of the spot centroid can be found by means of simple combinations of the 4 output signals.

2. MULTI-SPOT POSITION DETECTOR

The initial issues of concern for a video imager are typically three: resolution, sensitivity and frame rate. Image resolution is related to the number of pixels in a certain chip area. Sensitivity depends on the fill-factor, technology used and integrated circuitry. Frame rate is both dependent on the previous factors, the target image and the image software. If affordability and compactness are added as desirable features it is unlikely they will be altogether optimized on a single device. Therefore, a trade-off among these items proves necessary for each particular application.

In the case of a Hartmann sensor, the multi-spot detector can in principle be a conventional charge-coupled device (CCD) or a CMOS imager [8], however neither of them allows fast enough frame readouts, unless expensive specialized CCD's are meant. Furthermore, as already mentioned, both provide image outputs that must be further processed to find the spots centroids. In fact, some simplifications on an imager are very convenient for this particular sensor.

Once a relatively small number of spots suffice for the detection of aberrations present in most optical systems of interest, and since position of each spot - rather than intensity distribution - is the pursued parameter, image resolution can be exchanged for direct position sensing. For this purpose several CMOS pixel cluster architectures, devised as PSD's, have been studied and reported [9]. Figure 5 summarizes those

structures. The lateral-effect photodiode (LEP) has very poor performance due to the low sheet resistance available for the photocollecting layers in standard processes and high substrate noise. The chessboard structure solves the problem by having two appended resistive chains and discrete photodiodes, but introduces spatial sampling error, which is minimized in the spiral structure. The latter structures, although featuring a highly linear response, do not provide a well-defined center due to variations in the resistive network and geometrical asymmetries. The quad-cell (QC), on the other hand, does not exhibit a linear response, except at its very center, but provides excellent fill factor, large photosensitive elements for the same area budget and has a very well defined center, which is convenient when centering spots.

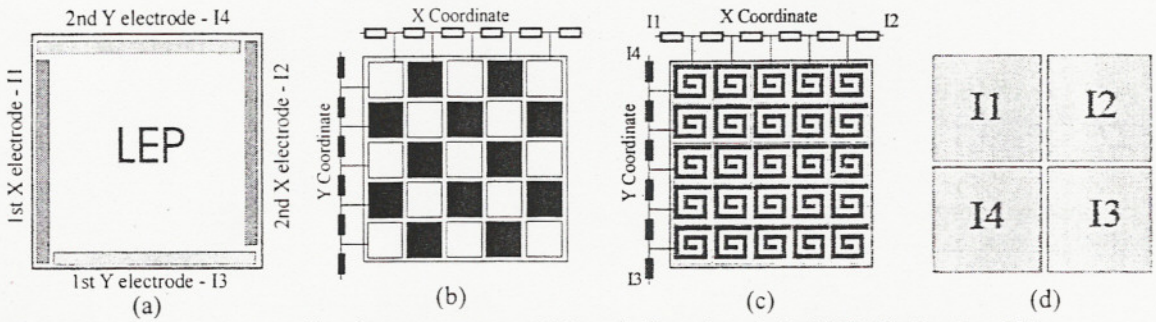

Figure 5: Various position-sensitive-detector structures. (a) lateral-effect photodiode (LEP), (b) chessboard-like structure, (b) juxtaposed spiral structure and the quad-cell.

The QC measures the position of one spot by simple mathematical calculations on the quad-cell signals, as suggested by Equations 1 and 2. The QC responses to spot displacements on x and y directions are given by x_{QC} and y_{QC}, which are normalized functions of the signals I_j, where j = 1, 2, 3 or 4. A multi-spot position detector is then achieved by integrating a number of QCs in a matrix, where the maximum allowed number of spots equals the number of QCs.

$$x_{QC} = \frac{(I_2 + I_3) - (I_1 + I_4)}{\sum I_j}. \quad (1)$$

$$y_{QC} = \frac{(I_1 + I_2) - (I_3 + I_4)}{\sum I_j}. \quad (2)$$

A four-channel parallel output, rather than a serial output, enables all four pixels of a QC to be addressed simultaneously, thus avoiding that temporal artifacts influence the position information. This contributes to faster frame readout as well. Then, instead of row and column decoders, as usual for imagers, it is more convenient to have a customized decoder to access each quad-cell at a turn.

Silicon CMOS technology offers a good deal for compactness and affordability by enabling both digital and analog electronic circuitry to be integrated on the chip and by being widely available. Nevertheless, state-of-the-art processes allow a very large amount of pixels and high circuit density, but have drawbacks for imaging as high stacks of layers and very shallow junctions, limiting light collection and sensitivity to longer wavelengths, respectively. In our case only a relatively small number of pixels is necessary, so they can be made large and more traditional processes will suffice. The main advantages are predictable behavior, deeper photo-collecting junctions, availability and lower cost.

Either active- or passive-pixel architectures [10, 11] can be chosen (Figure 6). The first drives the pixel signal faster to the output and reduces readout noise, but requires node-voltage reset, besides introducing fixed-pattern noise (FPN), which on its turn requires double sampling to suppress offset. On the other hand, the passive-pixel architecture introduces delay to the signal, once the junction capacitance is added to the transmission line capacitance but needs only the pixel-select control line and has virtually no FPN for large pixels, which is very convenient for zeroing of the spot position.

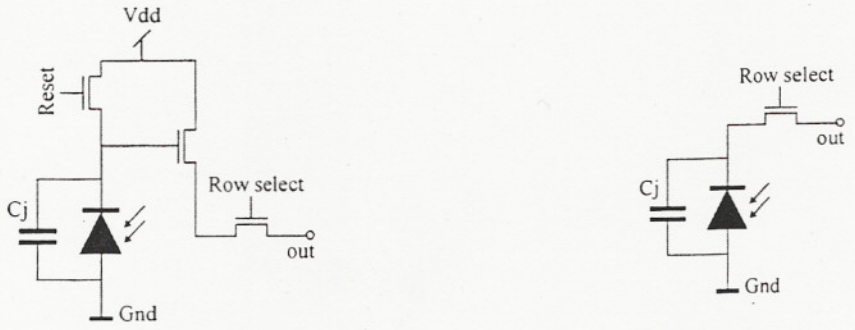

Figure 6: (a) Active- and (b) passive-pixels schematics. C_j is due to the photodiode intrinsic collection junction.

3. LAYOUT

3.1 Hartmann mask

The Hartmann mask was fabricated with sixty-four circular holes ($\phi = 450\mu m$) located in an 8x8 orthogonal grid with a 1000μm pitch (Figure 7). Every hole on the mask generates a wavelength-dependant spot intensity profile that changes with the distance between the mask and the observation plane (detector). A variation in the intensity profile leads to a different response curve of the quad-cell. In general the best fit for a response to a radially symmetric spot is the sigmoidal and the goodness-of-fit varies with the intensity profile. Using a computer model, we simulated the intensity profile resulting from the mask holes at various distances. Then, with a quad-cell model we estimated its response to each intensity profile and the best fit. It was found that the best results are achieved if the mask is placed at approximately 6cm above the detector plane, where the spot intensity profile is as shown in Figure 8.

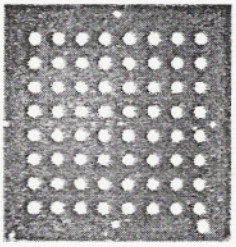

Figure 7: Photograph of the fabricated Hartmann mask.

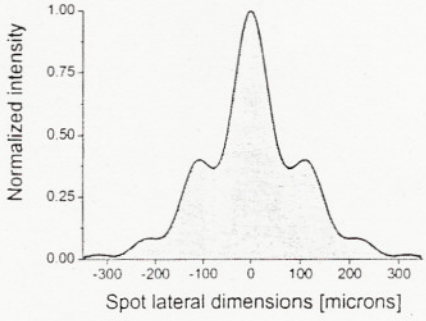

Figure 8: Cross-section of the radially symmetric spot profile on the detector plane, placed 6 cm under the mask.

3.2 Detector

The detector consists of 256 pixels clustered four by four, so that an orthogonal array of 64 quad-cells (QCs) is formed. The chip has an integrated analog demultiplexer and a sampling-rate controller, which allows random access to QCs and either 4 or 8 parallel outputs at a time. A diagram with the detector layout is shown in Figure 9. There are two groups of QCs, those in the inner region and those in the outer region. Digital circuitry has been placed around the sensor matrix. The demultiplexer is spread over the chip, with the analog part integrated into every pixel and the digital decoders separated into two modules: one for the outer and another for the inner QCs. The sampling-rate controller can redirect the inner-region decoder to address outer QCs too.

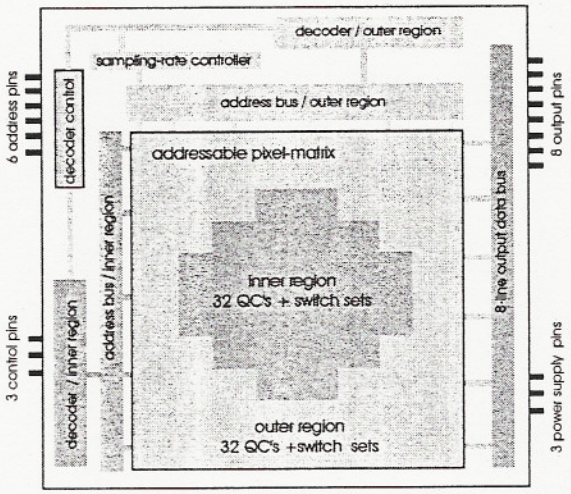

Figure 9: Layout of the different modules present on chip.

4. IMPLEMENTATION

A $1cm^2$ CMOS chip was implemented in a 1.6μm double-metal single-poly n-well process. Each QC consists of four 300μm x 300μm passive pixels (94% pixel fill factor), each with an attached switch set, seen as a white dot on an external corner of each pixel in Figure 10.

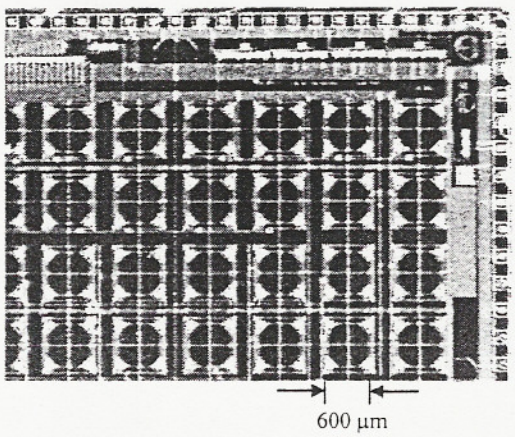

Figure 10: Detail of the fabricated CMOS chip. The whole chip occupies a $1cm^2$ area.

Each pixel has two photodiode junctions: p^-/n-well and n-well/p^--epilayer as is depicted at the cross section of a QC in Figure 11a. The photocurrent is read through an n^+ ohmic contact to the n-well in integration mode. The connection of the junctions is shown in Figure 11b. There is a 380μm gap between QC's so to minimize interference between carriers generated by neighboring light spots.

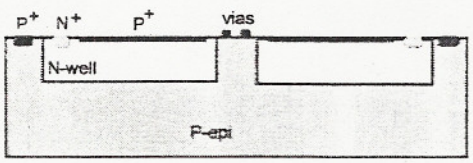

(a)

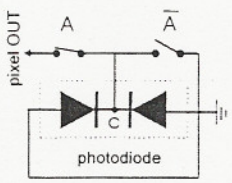

(b)

Figure 11: (a) Cross-section of one quad-cell; (b) photodiode connection.

A switch set is based on analog transmission gates that either transfer the photocurrent to the output bus or discharge the pixel. They have been designed with charge attenuation and a digital inverter (Figure 12). The demultiplexer is split into several digital modules around the QC array, which control the analog data transmission at the on-pixel switch sets. Placement of most electronic circuitry at the edge of the chip ensures less signal crosstalk through the substrate. The sampling-rate controller is a switch batch that leads the digital control signals to a single QC region or to both regions.

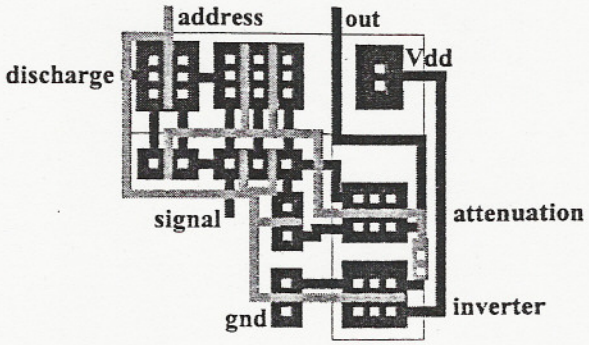

Figure 12: Switch set layout.

5. OPERATION

If a quad-cell is selected by the QC-select line all its four photodiodes transfer their photocurrents to the corresponding output lines (Figure 13), which happens in integration mode. An analog switch assures optimal current transfer and has a 10μs settling time.

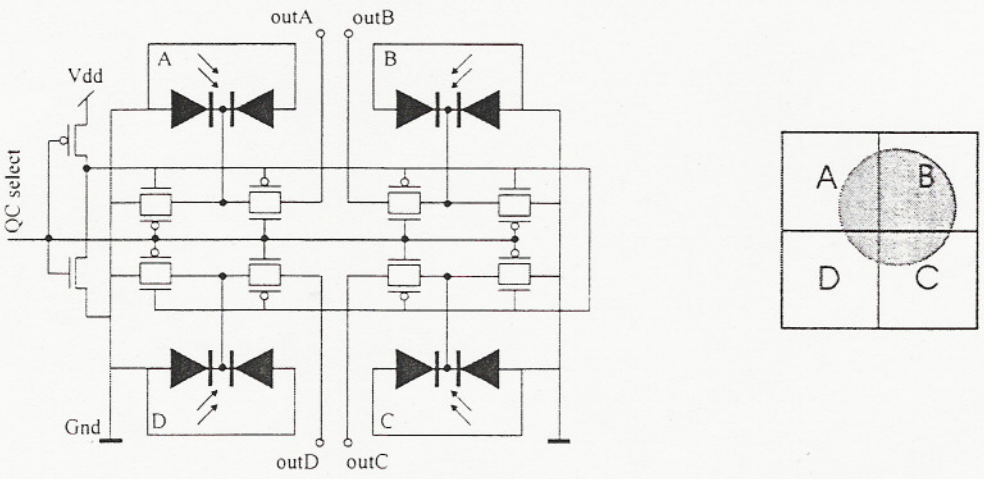

Figure 13: Schematics and arrangement of pixels in a quad-cell. The gray circle represents a light spot on the QC.

Coupled and uncoupled operational modes are possible (Figure 14). In the first, every QC in the inner region is coupled to another one in the outer region, i.e., they are addressed simultaneously and 8 signals (4 from each QC) are sent to output terminals at a time. In this case a 5-bit address register is used. Conversely, in the uncoupled mode any QC in the whole chip is enabled by a 6-bit address and 4 signals are available at the output. Random QC addressing is possible in both modes. It gives the flexibility to, for instance, vary the number of amplifiers at the output and to zoom in a certain region of the array.

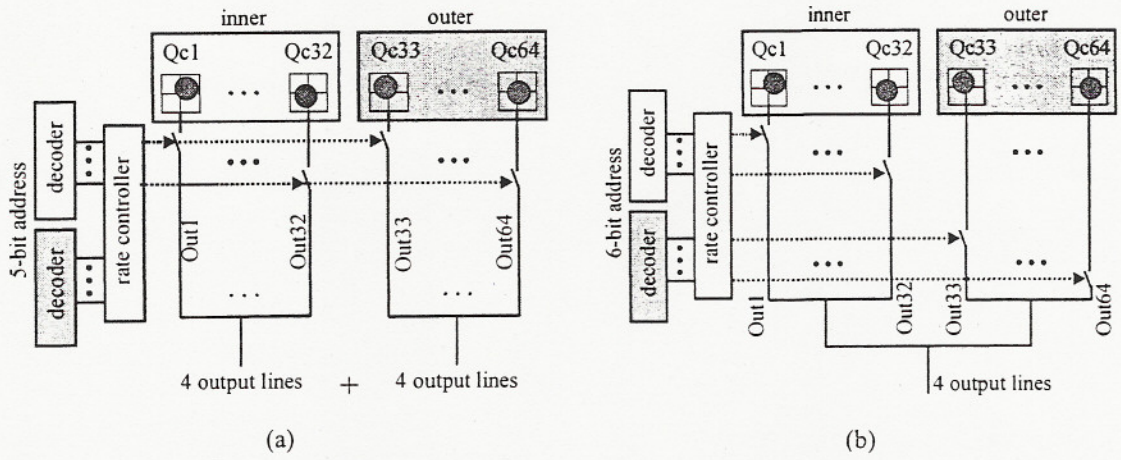

Figure 14: (a) Coupled and (b) uncoupled operational modes. Each data line from a given QC in the picture represents 4 parallel lines been addressed simultaneously. The dotted lines are digital control lines to operate the switches.

6. EXPERIMENTAL SETUP

Test photodiodes and quad-cells have been fabricated on chip. They enable us to measure the sensor characteristics without the influence of electronic circuitry. Spectral response of the light sensitive cells, quantum efficiency and dark current are extracted from them. Other parameters as wavefront sensitivity and operational speed are estimated too.

The photodiode spectral response was measured with the setup shown in Figure 15, which consists of a light source, a collimating lens system and a monochromator.

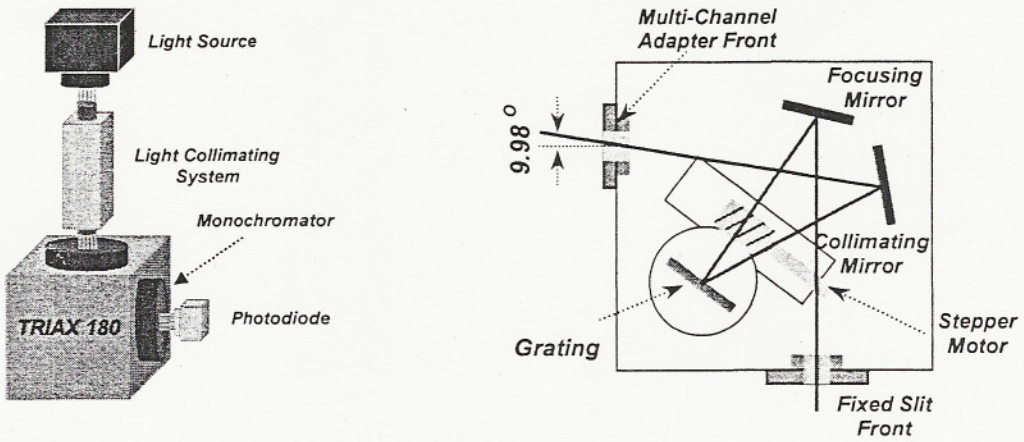

Figure 15: Experimental setup for measurement of the spectral response of the photodiode.

A 150 W Xe lamp was used as light source. It has a spectrally flat characteristic in the wavelength range between 400 nm and 700 nm with optical power of about 10 mW $m^{-2}nm^{-1}$ (irradiance at 0.5m). To obtain a scan over the desired spectral range (400 nm – 700 nm) a TRIAX 180 Imaging Spectrometer was used as a Monochromatic Illuminator. With the light source coupled to an entrance slit, the TRIAX 180 provides a specific band-pass at the exit. Changing the slit widths can vary the spectral band-pass. The wavelength accuracy is ± 0.3nm (slit width = 1mm). The stray light signal, caused by scattering or re-diffracted light inside the monochromator, is about 3 x 10^{-4} of the primary light signal. The scan drive facilitates tuning the

central wavelength of the exiting beam. A computer using IEEE488 interface controls the slits, scanning drive and shutters remotely. Direct photodiode output current was measured for each wavelength step. Hamamatsu photodiode S1226 was used for calibration. It is seen in the previous figure that the light beam leaves the spectrometer at an angle of 9.98 °, which together with possible misalignments on the photodiode suggests that the angle at which the beam reaches the photodiode surface does differ from 0 °, which has to be taken into account in the interpretation of the results.

For further measurements we used a He-Ne 633nm laser. The laser beam was first expanded and then filtered by a 12mm aperture. The quantum efficiency for this wavelength was measured by focusing a spot, of known intensity power on a photodiode of the test quad-cell and by measuring its output current. By blocking the spot, dark current at room temperature was found. No bias has been applied in either case.

To measure the characteristics of the system we placed the Hartmann mask with circular holes at a 6cm distance from the detector plane. Once there is enough space between neighbor QCs and considering the intensity profile of each spot, lateral interference plays no major role. The sensor was attached to an x-y stage. All results were obtained in the coupled mode and an operational transimpedence amplifier was used for each of the eight output lines. The output voltages were then read by means of a multi-channel data-acquisition card. By selecting a single spot on the mask and with aid of the x-y stage we scanned the QC surface and obtained its response to different spot positions. Operational speed was obtained by measuring the charge time of a photodiode located at the far end of a data transmission line. Wavefront sensitivity was computed as the rms deviation of the difference between two consecutive measurements of the same wavefront, for a certain number of Zernike terms.

7. PERFORMANCE

7.1 Quantum efficiency and dark current

Noise levels are technology dependant, and especially when one aims at standard process, very few degrees of freedom are available to minimize them. Guard rings are a standard way to avoid large substrate noise interference between circuitry and sensor modules. One possible solution is to try circuit approaches that will cancel out some noise contributions, mostly increasing complexity and possibly reduce sampling speed. Both FPN and kTC noise can be treated by this method. FPN is not present in our case, due to the large size of the photodiodes, compensating switches and absence of output buffers. Yet, kTC noise might have some contribution, but before considering to introduce complexity to the system to suppress it, it might be worth checking whether the quantum efficiency is optimized for a desired wavelength. Several applications allow the employment of a red laser (λ=633μm) as the probe beam and have enough light available, which suggests that investigation for this wavelength is sensible.

Junction depths are pre-defined for a certain CMOS process: the lower the feature size, the shallower the junctions. It means lower quantum efficiency for higher wavelengths. A non-submicron standard process usually has an n-well depth of about 3μm, which is enough for quantum efficiency between 40 and 60%, with doping levels optimized for electronics. We, however, measured it as been at the lower end at about 40%, for λ = 633nm. An important consideration is that not only photoelectron generation and collection is critical in determining the quantum efficiency but also the dielectric layers, which might inadvertently function as poor optical coatings on top of the sensitive region. The influence of these layers as well as an appropriate optimization will be tackled in a subsequent subsection.

Although usually regarded as background contribution to noise, in several cases the dark current, which is temperature dependant, limits the signal-to-noise ration (SNR). In standard CMOS the p+ implantation does not have enough doping to work as an inverting layer for a pinned photodiode [12], in order to reduce dark current considerably. Also, sophisticated interface planarization and reduction of surface traps is costly and introduces non-standard steps. Thus, practically nothing can be done to reduce dark current if the process is to be kept standard. Dark current was found to be 0.5 nA, at room temperature.

7.2 Spectral response

In the CMOS standard process we used, there are several layers upon a photodiode that can influence its spectral response, namely the gate oxide, TEOS, BPSG, plasma oxide and passivation layer. In order to obtain a device with good response for a given wavelength, these layers must be taken into account.

Figure 16 shows a thin-film stack with q interfaces, i. e. q-1 films. Film i has a light wave traveling to the right, E_i^+, and another traveling to the left, E_i^-. These waves make an angle θ_i relatively to the normal of the interface. Each film has a refractive index n_i (a complex number in the case of absorbing films), and a thickness d_i (not in the figure). Film 0 is the substrate and film q is the input medium normally constituted by air. Considering all thin-film layers, the electrical fields of incident, reflected and transmitted waves are respectively E_q^+, E_q^- and E_o^-. Only these fields have practical interest in order to calculate the film stack behavior.

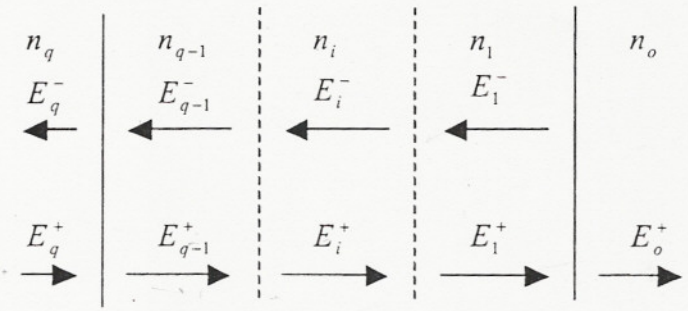

Figure 16: Parameters for a thin film stack.

The phase thickness of film i is given by $g(i) = \dfrac{2\pi u_i d_i \cos\theta_i}{\lambda}$, where d_i is the film thickness, λ is the wavelength of light in free space, the angle θ_i is given by Snell's law and

$$u_i = \begin{cases} (n_i - ik_i)/\cos\theta_i & for \quad p \quad polarization \\ (n_i - ik_i)\cos\theta_i & for \quad s \quad polarization \end{cases}, \tag{3}$$

where n and k are the refractive index and the extinction coefficient of the medium, respectively. Phase thickness represents the change in phase of the wave when it goes through the film [13].

The boundary conditions at each side of the interface are derived from the electromagnetic theory: the components of electric filed and magnetic field vectors parallel to the interface must be the same at both sides. By using this conclusion and considering the phase change in film i, the equations for electric and magnetic fields become

$$\begin{bmatrix} E_{i+1} \\ H_{i+1} \end{bmatrix} = \begin{bmatrix} \cos g_i & i\sin g_i / u_i \\ ju_i \sin g_i & \cos g_i \end{bmatrix} \begin{bmatrix} E_i \\ H_i \end{bmatrix}. \tag{4}$$

As $H_i^{\pm} = \pm u_i E_i^{\pm}$, $E_i = E_i^+ + E_i^-$ and $H_i = H_i^+ + H_i^-$, [14]

$$\begin{bmatrix} E_q^+ \\ E_q^- \end{bmatrix} = \frac{1}{2}\begin{bmatrix} 1 & 1/u_q \\ 1 & -1/u_q \end{bmatrix} \begin{bmatrix} E_q \\ H_q \end{bmatrix} \text{ and } \begin{bmatrix} E_o \\ H_o \end{bmatrix} = \begin{bmatrix} 1 \\ u_o \end{bmatrix} E_o^+, \text{ since } E_o^- = 0. \tag{5}$$

The reflection and transmission coefficients for the thin-film stack are

$$r = \frac{E_q^-}{E_q^+} \quad , \quad t = \frac{E_o^+}{E_q^+} \, . \tag{6}$$

The reflectance and transmittance are given by

$$R = |r|^2 \quad \text{and} \quad T = \frac{u_o}{u_q}|t|^2 \, . \tag{7}$$

A simulation of the thin film stack on the photodiode was made using Equations 4, 5, 6 and 7 and was based on the optical database provided by Sopra S.A.; variations of the incident angle, due to misalignments of the photodiode fixture are considered too. The film stack is composed of Si_3N_4 (800nm), plasma oxide (800nm), BPSG (600nm), TEOS (100nm) and gate oxide (25nm), where the number in parentheses is the approximate thickness. The result, transmission as a function of wavelength, is shown in Figure 17 by the thinner line. The experimental results on the spectral response of the photodiode are plotted as a thicker curve on the same graph. As can be seen, the response of the photodiode depends directly on the amount of light transmitted through the dielectric layers. Differences between the theoretical transmission peaks and experimental spectral response results can be attributed to variations in layer thickness during the fabrication process. Nevertheless, peaks match within 13nm. These results are an indication for the lower than expected quantum efficiency. For $\lambda = 633$nm, the transmittance as well as the photodiode response is completely off the peak, which can be translated into a poorer quantum efficiency.

Due to dielectric layer thickness variations between two different batches, especially for the plasma oxide, considerable changes in peak positions are observed. Since the peaks are rather sharp, reproducibility of results is compromised. Further simulation results show that a reasonable response in red region (633nm) can be achieved if passivation and plasma oxide layers are etched from the photodiode structure. Although the maximum achievable transmittance is lower than the maximum for a full dielectric stack, it has the advantage of being broader, thus attributing more uniformity to the spectral response. It is however still prone to variations between batches, because of the absence of an appropriate etch stop. Figure 18 shows the transmittance for the minimum, maximum and ideal thickness within the process uncertainty window. Even for the worse case (minimum thickness), the transmittance has a small improvement in relation to the present results. The transmittance for an ideal thickness of 545nm is about 0.8. The only way to achieve this is by a very careful control of the etching time, usually not necessary in a standard process due to structural etch stops at the via/contact etching sites. A similar result, with an even broader response, can be obtained if only TEOS and gate oxide are left, which can only be accurately achieved if an additional etch stop is defined on the photodiode region and then removed.

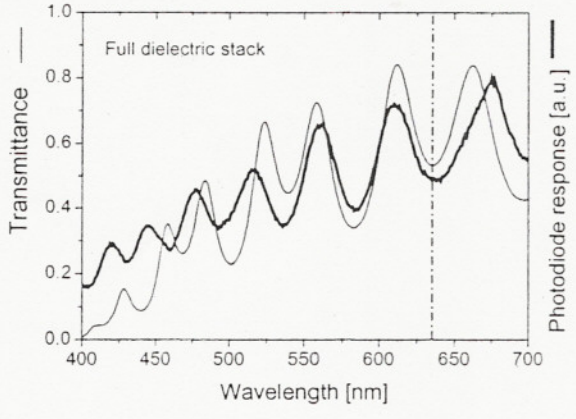

Figure 17: Simulated transmittance through full dielectric stack and measured photodiode spectral response.

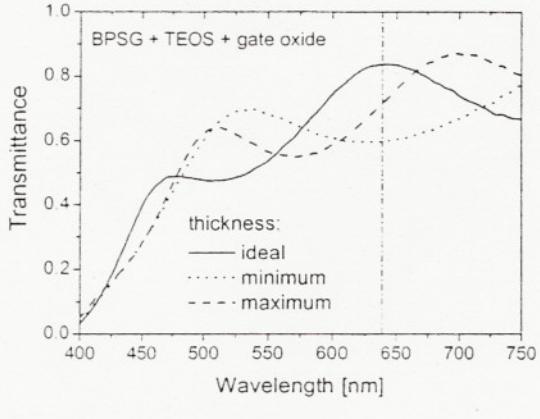

Figure 18: Simulated transmittance for three different layer thicknesses with only BPSG, TEOS and gate oxide.

7.3 Wavefront sensitivity

Sensor simulation shows that the error of reconstruction depends on the detector accuracy, spectrum of aberrations and number of terms used for reconstruction. In the case of low-spatial-frequency aberrations, the best reconstruction is achieved with a small number of terms, once introduction of higher-order terms produces a noisy solution. High-spatial-frequency aberrations, however, require a larger number of terms and will be therefore reconstructed with lower accuracy.

The sigmoidal response of a fabricated QC, for a 450μm 12μW spot is seen in Figure 19. The QC signal-to-noise ratio (SNR) depends basically on the intensity level and noise introduced by the amplification stage. When the spot centroid was confined to the central region of the detector and no data processing was made, we found that the SNR is 64dB for a 12μW spot and 25dB for a 0.2μW spot, including amplification noise. The latter figure can be improved considerably if data is averaged, at the expense of operational speed. Position accuracy for spot displacements up to 100μm about the QC center is as low as 1.4μm, when SNR=64dB. Preliminary tests with 9 Zernike polynomials and SNR = 65dB indicate that λ/20 RMS wavefront sensitivity is achieved.

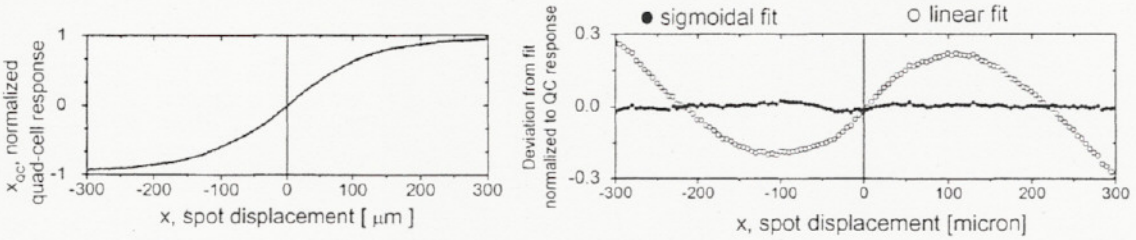

(a) (b)

Figure 19: a) response of a fabricated QC, for a 450μm 12μW spot; b) error in the sigmoidal and linear fits.

7.4 Frame rate

There are fundamentally two chief factors that dictate the achievable frame rate: photodiode charge time and switch settling time. The demultiplexer digital modules work so much faster than other modules that they are not an issue here. The photodiode charge time is related to its junction capacitance, which increases with the area. In our case $C_j \approx 50$ pF including the two used junctions. This leads to a full integration time slightly smaller than 10μs. The analog switch has a transient behavior when turned ON/OFF. It is due to accumulated charge bouncing back and forth on either side of the transistors channels. The charges reach a steady state after approximately 10μs, matching conveniently the photodiode integration time. Therefore, pixel readout frequency is 100 kHz and when the sampling-rate controller sets the sensor to the coupled mode, the frame rate is about 3 kHz. The overall system frequency, however, might be reduced due to data-acquisition time, data processing, reconstruction and eventually adaptive mirror control in close-loop.

8. CONCLUSIONS

We successfully fabricated a customized CMOS Hartmann wavefront sensor, with position-sensitive detectors, able to accommodate up to 64 spots about an orthogonal grid. It features random access to position information of each spot. Quantum efficiency of the photosensitive elements is 40%, and is so far dependant on the process batch. Simulations show that etching of appropriate dielectric layers, still conforming to a standard process, might increase the uniformity region of the spectral response and offers at least a small improvement to the transmittance. Maximization of the transmittance is dependant on an

accurate control of the layers thickness, which can be achieved if extra process steps are added. When enough light is available, each position-sensitive detector features 1.4μm position accuracy, which in preliminary tests lead to λ/20 rms reconstruction accuracy. The sensor was designed to allow frame rates up to 3kHz. If operated along with optimized computer algorithms and appropriate data-acquisition hardware, the overall operational frequency will be suitable for real-time applications.

ACKNOWLEDGEMENTS

The authors are thankful to the Dutch Technical Foundation for the support of this project since January 2001 (DOE.5375) and to Delft Technology Center (DTC / DIMES) staff, especially Ing. Hugo Schellevis for some useful information.

REFERENCES

1. G. Love, *Adaptive Optics for Industry and Medicine*, World Scientific Publ. Co., Durham, 2000.
2. J. Liang, D. Williams, D. Miller, "Supernormal vision and high-resolution retinal imaging through Adaptive Optics", *J. Opt. Soc. Am.*, **A14** (11), pp.2884-2892, 1997.
3. D. Neal, T. O'Hern, J. Torczynski, M. Warren, R. Shul, T. McKechnie, "Wavefront sensors for optical diagnostics in Fluid Mechanics", *Proc. SPIE* **2005**, pp.194-200, 1993.
4. G. Vdovin, S. Middelhoek and P. Sarro, "Technology and applications of micromachined silicon adaptive mirrors", *Optical Engineering* **36**(5), pp.1382-1390, 1997.
5. M. Loktev, D.W. de Lima Monteiro and G. Vdovin, "Comparison study of the performance of piston, thin plate and membrane mirrors for correction of turbulence-induced phase distortions", *Optics Communications* **192**, pp.91-99, 2001.
6. J. Geary, *Introduction to Wavefront Sensor,* SPIE Press, 1995.
7. D. Noorlag, *Lateral-photoeffect Position-sensitive Detectors,* PhD Thesis – Delft University Press, Delft, 1982.
8. S. Mendis et al, "CMOS active pixel image sensors for highly integrated imaging systems", *IEEE J. Solid-State Circuits* **32**(2), pp.187-197, 1997.
9. D. W. de Lima Monteiro et al., "Various layouts of analog CMOS optical position-sensitive detectors," *Proc. SPIE* **3794**, pp.134-142, 1999.
10. E. Fossum, "Active-pixel sensors – are CCD's dinosaurs?", *Charge-coupled devices and solid-state optical sensors III, Proc. SPIE* **1900**, pp.2-14, 1993.
11. E. Fossum, "CMOS Image Sensors: Electronic Camera-On-A-Chip", *IEEE Trans. Electr. Devices* **44**(10), pp.1689-1698, 1997.
12. T. Lulé et al, "Sensitivity of CMOS based imagers and scaling perspectives", *IEEE Trans. Electr. Devices* **47**(11), pp.2110-12122, 2000.
13. D. Poenar, *Thin Film Colour Sensors*, PhD Thesis, Delft University Press, Delft, 1996.
14. H. Macleod, Thin Film Optical Filters, 3rd Edition, Institute of Physics Publishing, London, 2001.